Published in final edited form as:
Pattern Recognit. 2013 July 1; 46(7): 1933–1948. doi:10.1016/j.patcog.2013.01.011.

Directional Histogram Ratio at Random Probes: A Local Thresholding Criterion for Capillary Images

Na Lu[a,c], **Jharon Silva**[b], **Yu Gu**[c], **Scott Gerber**[b], **Hulin Wu**[c], **Harris Gelbard**[d], **Stephen Dewhurst**[b], and **Hongyu Miao**[c,*]

[a]State Key Laboratory for Manufacturing Systems Engineering, Systems Engineering Institute, Xi'an Jiaotong University, Xi'an Shaanxi, China

[b]Department of Microbiology and Immunology, University of Rochester, Rochester, NY, U. S

[c]Department of Biostatistics and Computational Biology, University of Rochester, Rochester, NY, U. S

[d]Department of Neurology, University of Rochester, Rochester, NY, U. S

Abstract

With the development of micron-scale imaging techniques, capillaries can be conveniently visualized using methods such as two-photon and whole mount microscopy. However, the presence of background staining, leaky vessels and the diffusion of small fluorescent molecules can lead to significant complexity in image analysis and loss of information necessary to accurately quantify vascular metrics. One solution to this problem is the development of accurate thresholding algorithms that reliably distinguish blood vessels from surrounding tissue. Although various thresholding algorithms have been proposed, our results suggest that without appropriate pre- or post-processing, the existing approaches may fail to obtain satisfactory results for capillary images that include areas of contamination. In this study, we propose a novel local thresholding algorithm, called directional histogram ratio at random probes (DHR-RP). This method explicitly considers the geometric features of tube-like objects in conducting image binarization, and has a reliable performance in distinguishing small vessels from either clean or contaminated background. Experimental and simulation studies suggest that our DHR-RP algorithm is superior over existing thresholding methods.

Keywords

Image thresholding; Random probe; Directional histogram ratio; Two-photon imaging; Whole mount microscopy; Capillary

1. Introduction

Modern imaging techniques such as two-photon and whole mount microscopy enable us to gain new insights into vascular architecture and development, both in normal tissue and in

Corresponding Author: Hongyu Miao, Ph.D., Dept. of Biostatistics & Computational Biology, University of Rochester, Rochester, NY, 14642, hongyu_miao@urmc.rochester.edu, Phone: 585-275-0408, Fax: 585-273-1031.

disease settings such as cancer [1–5]. Whole mount microscopy emerged almost a decade ago as a powerful, simple and relatively low cost method for assessing the three-dimensional structure of blood vessels, and for determining effects of local cytokine expression on tumor vasculature [3]. This represents a marked improvement on conventional immunohistochemistry of tissue sections, which yields only two-dimensional information. In addition, two-photon imaging is a comparatively new technique [6] that allows one to visualize three-dimensional living tissues using fluorescent dyes, and provides important advantages over traditional techniques such as confocal microscopy (e.g., greater tissue penetration depth and lower phototoxicity) [7].

To interpret complex vessel image data, a number of independent studies have proposed various morphological measures to quantify vessel plexus, including vessel length distribution, vessel radii/diameter distribution, vessel direction, vessel area/volume density, vessel branching point density, vessel branching angles, vessel endpoint density, fractal dimension etc. [8–18]. Obviously, the accuracy of these metrics heavily depends on the outcome of image processing (e.g., denoising, segmentation, and skeletonization). Unfortunately, local contamination of image data could occur in capillary images due to background staining, vascular leak or dye diffusion through vessel walls into surrounding tissues. In this case, it can become challenging to reliably define and map dense vessels (especially smaller vessels such as capillaries) in such images. A large number of vessel segmentation or extraction methods have been proposed in previous studies. For convenience, six categories of vessel segmentation methods (pattern recognition based, model based, tracking based, artificial intelligence based, neural network based, and tube-like object detection based approaches) have been reviewed in [19]. Also, segmentation techniques primarily for 3D vessel images have been discussed in [20]. Using the methods mentioned above (e.g., Amira or VidaSuite [21]), research on 3D highly-complex vessel network analysis has become feasible [15, 18, 22, 23]. However, we notice that the binarized version of a vessel image is usually required before extracting the skeleton/ridge of vessels, or detecting the contour of the vessels using deformable models. Also, before using some vessel segmentation methods, one or more thresholding procedures may need to be performed [21]; for example, Socher's method [24], a marginal space learning approach using hierarchical classifiers, needs to find edges at the first level of hierarchy and the edge detection accuracy could significantly benefit from the removal of contamination regions using thresholding algorithms. In addition, certain issues in vessel image thresholding have not been sufficiently addressed, as suggested in this study (Result section). Therefore, improved or new thresholding algorithms for specific problems still keep emerging [25–29]. In this study, we aim at developing a new and more accurate thresholding method that can deal with both clean and heavily contaminated vessel images.

1.1 Related Work

There are a wealth of thresholding methods, which can be classified as either global [26, 30, 31] or local approaches [32] based on whether the local neighborhood information of a pixel/voxel is used. Alternatively, depending on the type of information employed, such methods can be also classified as histogram shape-based [33–37], clustering-based [25, 38–42], entropy-based [43–48], attribute-similarity-based [49–51], spatial distribution-based [52–54] or local statistics-based approaches [55, 56]. The histogram-based methods calculate a threshold according to the shape of the intensity histogram. The clustering-based methods use similarity or dissimilarity measures to distinguish the foreground from the background [38]. Entropy-based methods determine a threshold by maximizing the entropy of the binary image [45, 57] or minimizing the cross-entropy between the original image and the resulted binary image [44, 58]. The attribute-based methods evaluate the difference between the original image and the binarized outcome based on attributes such as edge,

shape, gray level moments etc. [28, 49, 59]. These methods seek to preserve the geometric features of the raw image to the maximum. Spatial distribution-based methods mainly make use of the neighbor dependency among pixels, such as the co-occurrence matrix and the second order statistics. The strategy is to minimize the distributional variation from the original image to the binarized version [43]. The local statistics-based methods compute the threshold for a single pixel or a sub-window based on the local variance or contrast [60, 61], which usually result in different thresholds for different sub-windows [62]. Besides the well-classified methods above, alternative techniques such as fuzzy set [63, 64], evolutionary optimization [27], hybrid optimization [65], have also been proposed for image thresholding. Nevertheless, the basic ideas of these methods are similar to the six categories of thresholding methods described before and thus are not further discussed.

Unfortunately, the global thresholding algorithms usually cannot preserve object details properly, which could significantly compromise the robustness of outcomes. The local approaches can better preserve local details, but the size of the local region could have a great influence on the algorithm performance. The histogram-based methods are conceptually simple but only effective when the background and foreground are well separated in a raw image. When the histogram profile shape gets sophisticated (e.g., multiple peaks), the performance of such methods is likely to become unacceptable. For capillary images, noise pixels/voxels due to dye diffusion will have a high intensity such that they can be easily misclassified as foreground by the histogram-based methods. The attribute similarity-based methods heavily depend on how well the geometric attributes are extracted and thus are sensitive to image contents and associated attribute extraction methods. Due to the complexity of the geometric shapes of vessel plexus, the attribute (e.g., edge) based methods are difficult to apply. The clustering-based methods are among the most popular thresholding methods [25]. For example, the Otsu method and its variations [25, 38, 66], which seek the optimum threshold by minimizing the within class variance of foreground and background, have been implemented as automatic thresholding methods in prevailing image processing packages such as MATLAB™ [25]. Kittler's method is another popular clustering-based technique, which outperforms many other thresholding algorithms according to a recent survey [32]. However, our preliminary results (not shown) suggest that these clustering methods cannot generate satisfying results for the contaminated vessel images because the cloud of noise pixels/voxels has nearly the same intensity as that of vessels. The local statistics-based methods could perform well for certain local areas, but in general, such methods are not designed to distinguish meaningful objects from noise by shape. Besides the thresholding methods mentioned above, additional approaches have also been proposed for vessel segmentation [67, 68]; however, problems such as labor-intensive and subjective manual parameter tuning could be a serious issue for such approaches. For convenience, we summarize the representative thresholding methods in Table 1.

1.2 The DHR-RP Approach

Due to the unsatisfactory performance (or failure) of existing thresholding algorithms for capillary images, we propose a novel local adaptive method for vessel image thresholding in this study. The key idea of our method is to explicitly take the geometric feature of vessels into consideration such that the level of local background contamination can be automatically detected and an appropriate threshold can then be chosen. Specifically, after dividing the whole image into sub-windows, we use random probes (RP) to sample each sub-window; then a directional histogram ratio (DHR) at all the probes is calculated as an indicator of the existence of tube-like objects as well as the contamination level. The proposed DHR-RP criterion is also theoretically justified to illustrate why it can serve its purpose. It turns out that our new thresholding algorithm outperforms a number of existing methods, including the highest ranked Kittler's method in Sezgin and Sankur [32]. Also, the

proposed method can be easily adapted to other types of images with tube-like objects, such as the retina image [69], the brain MRI image [70], the yarn image [71], and the aerial road image [68].

Related researches on the use of geometric feature of vessels mainly include local binary pattern (LBP)[72], ray-casting features [73, 74] and rod-filtering [21]. LBP and the proposed DHR method share some similarity in choosing the neighbors of a pixel using a star-shape probe; however, LBP calculates the number of patterns at each neighborhood to obtain a texture spectrum, while our DHR-RP method counts the neighbors along each branch of the star-shape probe to obtain the directional distribution. The ray-casting feature technique casts equal-angularly rays from a pixel within the vessel to detect vessel walls and measures the centerness of the pixel. The rod-filtering method filters the vessel image by matching sub-blocks with rods at different orientations with the number of rods up to 82. Furthermore, although the concept of DH has been introduced before (e.g., to measure the thickness of an object along parallel directions [75]), the way we generate the directional histogram is different from the previous studies and our DH serves a different purpose. In short, the proposed DHR-RP algorithm is new and different from existing methods mentioned above although it also uses the geometric features of tube-like objects.

This paper is organized as follows. In Section 2, the contamination problem in capillary images is described in detail and the DHR-RP method is depicted for both 2D and 3D cases. In Section 3, the algorithm implementation is described. Experiment results are summarized and discussed in Section 4. In Section 5, we summarize this work and discuss its possible extension.

2. Method

2.1. Problem description

The whole mount and two-photon imaging can have a micron or submicron-scale resolution (e.g., [76]) and are thus suitable to small vessel visualization (i.e., the diameter of capillaries is 8 μm in average but could be as small as 3 μm [77]). However, capillary plexus has an extremely irregular and entangled network-like structure such that it is challenging to extract such vessels from a noisy background. In particular, in the contaminated region due to, e.g., dye diffusion, the area of the noise cloud could be 10 more times larger than the capillary diameter and the difference in intensity between the vessel and the noise can be small. For example, in Fig. 1(a), the area of the noise cloud is $130 \times 50\ \mu m^2$; in addition, the intensity of the pixels within the noise cloud varies from around 70 to 165 (in red), and the intensity of the vessel pixels ranges from around 80 to 200 (in red). It can be seen that the intensity of some noise pixels is even higher than that of the vessels. Such facts make the task of vessel extraction even more challenging. Unfortunately, existing thresholding methods cannot well address such a problem and thus either the small vessels in the contaminated region are thrown away or the contaminated background is misclassified as foreground. Consequently, the metrics (e.g., vessel length, area or volume) for interpreting vessel image data cannot be accurately calculated.

To better illustrate the problem, we use the vessel image in Fig. 1(a) as an example, where we can clearly see a contaminated region in the upper middle area. To extract the vessels from the background, we first apply the Kittler's method to the raw image and the result is shown in Fig. 1(b). Limited by space, we cannot try all existing thresholding methods here; therefore, the Kittler's method is used as a representative approach because it outperformed other 39 thresholding algorithms in different scenarios [32]. In Fig. 1(b), we see that, although all vessels are preserved, the contaminated region is also misclassified as foreground. To illustrate the problem of losing small vessels, we also apply the maximum

entropy method [78] to Fig. 1(a) and the result is shown in Fig. 1(c). We see that although the contaminated region is removed, however, together with a loss of the majority of true signals (vessels).

The problems illustrated above are not unique for capillary imaging. For example, similar problems have also been spotted in the retinal image analysis [69], the yarn image analysis [71], the road segmentation in aerial images [68], and many other images involving uneven illumination or artifacts. Therefore, it is necessary and useful to develop an adaptive local thresholding algorithm that can deal with both clean and heavily-contaminated regions in an image.

2.2. Directional histogram ratio at random probes

The directional histogram ratio at random probes (DHR-RP) algorithm consists of several steps, including background cleaning, sub-window division, DHR calculation for each sub-window, and threshold choosing for binarization etc.; for the complete procedure, the reader is referred to Section III. In this section, we mainly focus on the concept and calculation of DHR at random probes.

While noise pixels (or voxels) could randomly spread over the whole image, pixels (or voxels) from the same solid object will stay next to each other and are geometrically bounded; furthermore, an object always has a geometric shape, which could be either regular (e.g., square) or highly irregular (e.g., network-like entangled tubes). Such two simple facts are actually the basis of the DHR-RP algorithm. More specifically, we note that vessels are tube-like and thus the length of a vessel is (much) longer than its diameter. Given such a fact, one can expect that, within a circle centered at the major axis of a vessel, if the circle diameter is larger than the vessel diameter, the number of bright pixels/voxels one can sample along the major vessel axis direction could be much larger than that along the vessel diameter direction. However, within a circle in the noise cloud, the numbers of bright pixels/voxels sampled along different directions are expected to be close to each other since noise pixels/voxels randomly spread out. Therefore, the difference in the numbers of bright pixels along different direction could be an indicator that can reflects both the tube-like shape and the spatial distribution of noise. Based on this hypothesis, we develop the DHR-RP algorithm and we briefly summarize the key steps of this algorithm before we move onto its official formulation. First, we randomly spread a pre-specified number of probes into a sub-window of an image at positions that have a positive intensity. Second, at each probe location, we find certain neighbors of this probe along multiple different directions. Third, based on the neighbor pixel counts at all probes, we can generate a histogram with the number of bins being equal to the number of different directions, which is called directional histogram (DH). Finally, the difference in the pixel numbers along different directions is quantified as the criterion for choosing a threshold for image binarization.

For convenience, we first give the definition of d-neighbor, which has been described in some previous studies (e.g., LBP [72]).

Definition 1 (d-neighbor)—For two different pixels/voxels i and j in the same image (that is, $i \neq j$), let d denote the number of pixels/voxels between i and j along the straightline direction $i \rightarrow j$, pixel/voxel j is then called pixel i's d-neighbor in direction $i \rightarrow j$.

Note that the definition above is different from the conventional definition of neighbor for images in that a distance d is jumped. All the d-neighbors of pixel/voxel i constitute a d-neighbor set, denoted as $\mathbf{N}_i^d = \left\{N_{ij}^d, j=1, 2, \ldots, h\right\}$ $(j=1, 2, \cdots, h)$, where N_{ij}^d is the d-neighbor of pixel/voxel i in direction $i \rightarrow j$ and h is the number of different directions under

consideration. Before we move onto the definition of directional histogram, the concept of random probe should be introduced first. Simply speaking, a random probe is a randomly selected pixel (or voxel) that has a positive intensity; that is, we expect that both true signal (vessel pixel/voxel) and noise should have a positive intensity and thus we exclude the completely dark pixels/voxels (with an intensity of zero) from consideration as possible positions of probes.

Definition 2 (directional histogram)—For the i-th random probe ($i = 1,2,\ldots,n$), let I_{ij}^{d} denote the intensity of the d-neighbor in the j-th direction ($j = 1,2,\ldots,h$). A histogram with a total of h bins is called a directional histogram if its j-th bin is used to count the number of the d-neighbors of all the probes that are in the j-th direction and have a positive intensity ($I_{ij}^{d}>0$). For convenience, we let $\mathbf{H}^{d}=\{H_{j}^{d}, j=1,2,\cdots,h\}$ denote a directional histogram with

$$H_{j}^{d}=\sum_{i=1}^{n}\mathbf{1}\left(I_{ij}^{d}>0\right), \quad (1)$$

where $\mathbf{1}(\cdot)$ is the indicator function.

To better illustrate the two definitions above, Figures 2(a) and 2(b) show a probe and its d-neighbors for the 2D and 3D cases, respectively. In Fig. 2(a), the light pixel at the center is a randomly selected pixel, and the eight light pixels on the border are the 8 d-neighbors of the center pixel for $d = 3$. In Fig. 2(b), the light sphere at the center of the cube is a randomly selected voxel and all the light spheres on the cube surfaces are the d-neighbors of the center voxel for $d = 1$. Furthermore, if the center pixel in Fig. 2(a) and the center voxel in Fig. 2(b) are both probes, we can choose the 8 and 26 straightline directions from the center to the d-neighbors for the 2D and 3D cases, respectively. If the intensity of the d-neighbor of a probe in the j-th direction is positive (Fig. 2(a)), it then will be counted in the j-th bin of a directional histogram (e.g., j=1,2,…,8 for a 2D image and j=1,2,…,26 for a 3D image).

To describe the difference in the numbers of non-zero d-neighbors along different directions, we introduce the following definition, which is our criterion for choosing binarization threshold.

Definition 3 (directional histogram ratio)—The ratio between the maximum and minimum of a directional histogram is called the directional histogram ratio, denoted as

$$Dr=\frac{\max_{j}(\mathbf{H}^{d})}{\min_{j}(\mathbf{H}^{d})}.$$

Before we theoretically justify the criterion above, we need to discuss one particular geometric property of tube-like objects. For simplicity, we consider a 2D case as in Fig. 3. Let i be a pixel from a tube-like object O (shadowed) in an image (denoted as $i \in O$), and let j and k denote two d-neighbors of i in directions $i \rightarrow j$ and $i \rightarrow k$, respectively. In Fig. 3, $i \rightarrow j$ is chosen to be the vessel axis direction; also, if d is some distance larger than the local diameter of the tube, we can easily find a d-neighbor like k that falls outside of the tube in many directions (e.g., directions 1, 2, 3, 5, 6 and 7 in Fig. 3). Thus, for a tube-like object O in Fig. 3, we can expect that for any pixel $i \in O$, there exist two d-neighbors j and k in two different directions such that $j \in O$ and $k \notin O$; for a general tube-like object such as vessel, we can expect that this conclusion will still hold at least within a local region of the object. Furthermore, since pixel i falls on the object and thus has a positive intensity, it will be counted in the directional histogram bin which corresponds to the tube axis direction;

however, pixel k falls in the background and has a zero intensity such that it will not be counted in the histogram bin that corresponds to direction $i \rightarrow k$. Therefore, one can expect that for the directional histogram of a tube-like object, the number of non-zero d-neighbors counted in a certain bin (e.g., corresponding to the tube axis direction) will be much larger than that of other bins (e.g., corresponding to the tube diameter direction). Consequently, the directional histogram ratio (DHR) could be large and even goes to infinity for an ideal case such as in Fig. 3 since the minimum of the directional histogram is zero ($\min(\mathbf{H}^d) = 0$). However, for real vessel images with noise and multiple tube-like objects, $\min(\mathbf{H}^d)$ could be a small number but not exactly zero such that the DHR will become smaller. Therefore, the value of DHR could be an indicator of the existence of tube-like objects as well as the level of contamination in the background. To theoretically verify this, we consider two scenarios in capillary images: multiple tube-like objects with a clean background (***scenario 1***), and very few or no tube-like objects in a heavily contaminated region (***scenario 2***).

Proposition 1—Assume that all the objects in an image are tube-like and the spatial distribution of these objects is not isotropic with respect to all the directions used to generate the directional histogram, then $E(Dr) \gg 2$ for scenario 1 and $1 \leq E(Dr) < 2$ for scenario 2, respectively, where $E(Dr)$ denotes the expectation of the directional histogram ratio.

Proof—Let m denote the total number of pixels/voxels in an image, among which m_1 pixels/voxels are from the object (with positive intensity), m_2 are noise (with positive intensity) and m_3 belong to the background (with zero intensity). Also, let $\mathbf{M}_1$ denote the set of the m_1 pixels/voxels and $\mathbf{M}_2$ denote the set of the m_2 pixels/voxels, then the random probes will be selected only within the union $\mathbf{M}_1 \cup \mathbf{M}_2$ according to the definition of RP. The probability of the i-th RP ($i = 1,2,\ldots,n$) coming from the object is

$$p(i \in \mathbf{M}_1) = \frac{m_1}{m_1 + m_2}, \quad (2)$$

and the probability of RP being from noise is

$$p(i \in \mathbf{M}_2) = \frac{m_2}{m_1 + m_2}. \quad (3)$$

Let N_{ij}^d be a d-neighbor of RP i at a distance d. Ignore the possible spatial correlation between RP i and N_{ij}^d for simplicity, the probability of N_{ij}^d coming from an object satisfies the following inequality under the two assumptions given in the proposition

$$0 \leq p(N_{ij}^d \in \mathbf{M}_1 | i \in \mathbf{M}_1 \cup \mathbf{M}_2) \leq \frac{m_1}{m}, \quad j = 1, 2, \ldots, h, \quad (4)$$

where the lower boundary corresponds to the case in direction $i \rightarrow k$ in Fig. 3 and the upper boundary corresponds to the case in direction $i \rightarrow j$ in Fig. 3, respectively. Since noise can randomly spread over the whole image, the probability of N_{ij}^d being noise is

$$p(N_{ij}^d \in \mathbf{M}_2 | i \in \mathbf{M}_1 \cup \mathbf{M}_2) = \frac{m_2}{m}. \quad (5)$$

For a d-neighbor N_{ij}^d to be counted in the j-th bin of the directional histogram, it must have a positive intensity and thus could be either noise or from an object. Let A_{ij}^d denote the event that a N_{ij}^d is positive and counted in the j-th bin of the directional histogram, then the probability of event A_{ij}^d can be derived based on Eqns. (4) and (5) as follows

$$\begin{aligned} p(A_{ij}^d) = p(N_{ij}^d \in \mathbf{M}_1 | i \in \mathbf{M}_1 \cup \mathbf{M}_2) + p(N_{ij}^d \in \mathbf{M}_2 | i \in \mathbf{M}_1 \cup \mathbf{M}_2) \\ \Rightarrow \frac{m_2}{m} \leq p(A_{ij}^d) \leq \frac{m_1+m_2}{m}. \end{aligned} \quad (6)$$

The expectation of the total number of positive d-neighbors in the j-th bin of the directional histogram satisfies

$$\begin{aligned} E(H_j^d) = \sum_{i=1}^{n} p(A_{ij}^d) \cdot 1 \\ \Rightarrow n \cdot \frac{m_2}{m} \leq E(H_j^d) \leq n \cdot \frac{m_1+m_2}{m}. \end{aligned} \quad (7)$$

According to Eq. (7) and the definition of the directional histogram ratio, it can be easily verified that

$$E(Dr) = \frac{\max_j(E(H_j^d))}{\min_j(E(H_j^d))} = 1 + \frac{m_1}{m_2}. \quad (8)$$

For scenario 1, we have $m_1 \gg m_2$ and a small m_2 (e.g., approximately zero); based on Eq. (8), we have

$$E(Dr) = 1 + \frac{m_1}{m_2} \gg 2; \quad (9)$$

for scenario 2, we have $m_2 \gg m_1$ such that

$$1 \leq \left(E(Dr) - 1 + \frac{m_1}{m_2} \right) < 2. \quad (10)$$

In the proposition above, we consider two extreme scenarios and the DHR is shown to be very different for the two scenarios. It is difficult to consider a comprehensive scenario that can mathematically describe all possible vessel images due to the large stochasticity in vessel number, vessel spatial distribution, vessel diameter, and noise/contamination position and intensity; however, the proof above based on two simplified scenarios sufficiently illustrates why DHR works. We will further discuss the assumptions in Proposition 1 in the discussion section.

3. Implementation

Since the DHR-RP algorithm is a local method, we need to divide the whole image into a number of sub-windows first. In this study, a 2D rectangular window and a 3D cube are used for 2D and 3D images, respectively. Within each sub-window, the directional histogram can be generated by following the steps in Fig. 4, where rp is the counter of the

random probes and n is the pre-specified maximum number of random probes allowed in a sub-window. In the experiments of this paper, n is set to 100 unless specified otherwise. After a probe is randomly planted at a non-zero pixel/voxel, its d-neighbors are searched along the directions illustrated in Fig. 2. If the intensity of a d-neighbor is positive, 1 should be added to its corresponding bin of the directional histogram. For more details, please see Fig. 4.

After the directional histogram is generated, the directional histogram ratio needs to be calculated. As illustrated in the previous section, DHR is an effective indicator of both the existence of tube-like objects and the contamination level. More specifically, a large DHR value suggests the existence of tube-like objects as well as a low contamination level such that a small intensity threshold should be used for image binarization; accordingly, a large intensity threshold should be used for a small DHR value. According to proposition 1, we can compare the calculated DHR with 2 to judge whether the directional histogram ratio is large or small. That is, when the directional histogram ratio of a sub-window is larger than 2, a low threshold should be used; otherwise, a high threshold will be suitable. In practice, a number greater than 2 can be used if the contamination is not heavy; however, a value of 2 turns out to be able to well meet the performance requirement in this study.

Once it is verified whether a low or high threshold should be used for a sub-window, the remaining problem is how to calculate this local threshold for binarization. As mentioned in the introduction section, a number of methods have been developed in previous studies to calculate the binarization threshold and our DHR-RP method can be flexibly combined with any of such methods. For example, the Otsu method is a popular and widely implemented algorithm and is thus used in our current implementation. For simplicity, we applied the multi-level Otsu method [66] to the whole image to automatically obtain two thresholds as the high and low thresholds, respectively. Specifically, in the experiments of this paper, 3-level Otsu is employed and the lowest two levels have been adopted as the low and high thresholds. Furthermore, the multi-level Otsu method can be applied to each sub-window instead of the whole image such that a different set of high and low thresholds can be obtained for each local area. However, our experiments show that our simplified implementation can already achieve satisfactory performance. It should be mentioned that within one cube of a 3D image, the high and low thresholds need to be obtained from each different image slice.

The complete procedure of the proposed DHR-RP algorithm is shown in Fig. 5, where w_{max} is the total number of sub-windows and w is a counter of the sub-windows. Finally, it should be mentioned that a background cleaning step needs to be performed before entering the body of the DHR-RP algorithm, which simply sets the intensities of the dark pixels/voxels to zero if their intensities are smaller than, e.g., 5% of the intensities of the brightest pixels/voxels. This step can prevent the random probes from being planted in the clean background region. For fair comparison, the same background cleaning procedure has been applied before the execution of every method in comparison.

4. Result and discussion

We first validate the idea of the DHR-RP algorithm using a few sample images. Limited by space, the details of validation are included in the Supplementary Materials, but the results suggest that the DHR-RP algorithm behaves as predicted by the theories in Section 2.

4.1. Experimental results

4.1.1 Comparison with global thresholding methods—To verify the performance of the DHR-RP algorithm, we conduct a number of comparisons for capillary images of

different quality (specifically, 38 frames of brain vessel images from 4 mice). Limited by space, here we only report results from 3 representative images of different quality. In Figures 6(a), 7(a) and 8(a), we have a high-quality image, a moderately contaminated image, and a heavily contaminated image, respectively. More specially, Fig. 6(a) has nearly no contaminated region; Fig. 7(a) has a small but obvious contaminated region in the upper middle part; and Fig. 8(a) is heavily contaminated in the upper right corner and one can see contamination at many places.

The first set of comparisons we conduct are between our DHR-RP method and the existing global thresholding algorithms. We have not compared our method with some integrated vessel extraction methods, like those in VidaSuite [21] and VesSeg [29], because these tools employ a number of preprocessing (e.g. median filtering, Gaussian filtering and image enhancement) and post processing algorithms (such as erosion, dilation, gap filling) to obtain better extraction performance, which are thus not fair to be compared in our experiments. Limited by space, we only select six representative global algorithms here for comparison, including the Otsu method [38], Huang's method [63], the percentile method [31], the triangle method [79], the maximum entropy method [78] and Kittler's method [40, 41]. Some of these methods like Otsu are among the most widely used methods and have been implemented in both open-source software (e.g., ImageJ) and commercial packages (e.g., MATLAB™) [25, 32]; also, the Kittler's method is chosen as it was ranked the highest in a recent survey of thresholding methods [32]. For Fig. 6(a), we see that the DHR-RP method and the Otsu method generate comparable binarization results; as indicated in Figures 6(b) and 6(c), the two methods can both remove most of the noise and preserve the vessels well. However, Huang's method, the percentile method, the triangle method and Kittler's method tend to misclassify the noise as foreground, as shown in Figures 6(d), (e), (f) and (h); also, the maximum entropy method removes most of the vessels as well as noise, as suggested in Fig. 6(g). Thus, except for the DHR-RP and the Otsu methods, all other methods give unsatisfactory results even for the high-quality image in Fig. 6(a). For Fig. 7(a), we see that the DHR-RP method performs the best as almost all the other methods misclassify the contamination in the middle upper region as foreground, as shown in Figures 7(c), (d), (e), (f) and (h); the only exception is the maximum entropy method, which still removes both a majority of true signals and noise (Fig. 7(g)). One possible reason why the previous methods perform worse is that the intensities of some noise pixels are actually higher than those of the vessels nearby. Fig. 8 gives the thresholding results for a severely contaminated image, where the DHR-RP method turns out to be superior to the other methods because it obviously better deal with the contaminated region around the upper right corner.

4.1.2 Comparison with local thresholding methods—The DHR-RP method itself is a local adaptive algorithm, it is thus necessary to compare it with existing local thresholding methods. Again, we only select a limited number of representative methods for comparison, including Bernsen's method [80], the mean method [81], the median method [81], the MidGray method [81], Niblack's method [82], and Sauvola's method [83]. Since the local thresholding methods are designed to deal with local contamination, we only use the heavily contaminated image in Fig. 8(a) for performance comparison. For the previous algorithms, we first use the existing implementation in ImageJ with its default computing parameters to binarize Fig. 8(a). The results are shown in Fig. 9, where we can tell that the results are barely acceptable. The vessels extracted by Bersen's method are disconnected, dim, and shrunk in area; meanwhile, the rest five methods show serious misclassification problems. Among the six methods, we then select four methods of better performance for further comparison, including Bernsen's method, the mean method, the median method, and the MidGray method. We then finely tune the computing parameters of these four methods until the best results can be obtained based on our visual perception, and the tuned results are

presented in Fig. 10. We find that the outcomes of all the four methods are significantly improved after parameter tuning; also, the mean method can generate outcomes that are even better than the DHR-RP method at certain region (e.g. the lower right part in Fig. 10(c)). However, we also can tell from the result that the mean method fails to remove the noise in the upper right corner; also, the vessel width is clearly inflated by the mean method, which could result in biased calculation of image metrics such as the vessel area. Thus, in this case, we conclude that the DHR-RP method has a comparable performance to the mean method. We then further compare the DHR-RP algorithm with the mean method using the image in Fig. 11(a), where the contamination problem gets worse. Now we see that the DHR-RP method can still well separate the foreground from the background (Fig. 11(b)), while the mean method fails to remove the background contamination even after a fine tuning of its computing parameters (Fig. 11(c)). Note that when we apply the DHR-RP method to the sample images, we use the same set of computing parameters and the results turn out to be among the highest quality for all the cases considered so far. Thus, we may conclude that the DHR-RP algorithm is not sensitive to the computing parameters like other local methods.

4.1.3 Quantitative comparison—To quantitatively evaluate the performance of DHR-RP against other methods, we have manually labeled the vessel image in Fig. 7(a) as the ground truth (see supplementary Fig. 4 for the manually labeled image). We consider four evaluation criteria, including the misclassification error (ME), false positive rate (FPR), false negative rate (FNR), and the dice coefficient (DC). The misclassification error [28] is defined as,

$$ME=1-\frac{|B_O \cap B_T|+|F_O \cap F_T|}{|B_O|+|F_O|},$$

where B_O and F_O are the background and foreground of the ground truth image, respectively, B_T and F_T denote the resulted background and foreground after thresholding, and $|\cdot|$ denotes the cardinality of a set. The dice coefficient [84] is defined as

$$DC=\frac{2TP}{(FP+TP)+(TP+FN)},$$

where TP, FP and FN denote true positive, false positive and false negative, respectively. DC is always between 0 and 1, with a value closer to one meaning a higher agreement with truth. In Table 2, the performance of the DHR-RP method versus several other global and local methods is given for one specific image sample Fig. 7(a). Among these seven methods in comparison, the proposed DHR-RP algorithm has the smallest misclassification error (2.48%), clearly suggesting a superiority of our DHR-RP method over the rest methods on the analyzed dataset. Although the DC of the maximum entropy method (0.96) is larger than that of the DHR-RP method (0.90), the FNR of the maximum entropy method is extremely high (98%), which suggests that this algorithm misclassifies almost all the vessels as background. Therefore, the overall performance of the DHR-RP algorithm is actually the best for the selected image sample in Fig. 7(a).

4.1.4 Simulation study—To confirm the superior performance of the DHR-RP method, we conduct an extensive simulation study. Without loss of generality, we add contamination regions (CR) to the image in Fig. 7(a) to generate simulated samples as follows (see Fig. 6 in

Supplementary Materials). First, each 1000 images are generated with 1, 2, 3, 5, 10 or 15 CRs, respectively (thus, 6000 images are generated in total). Second, since both background staining and vessel leaking can lead to contaminations, the positions of all CRs are randomly chosen so the CRs will not just stay around vessels. Third, considering that the areas of real CRs can vary from one local region to another, the area of each CR in the simulated images is randomly picked from a uniform distribution between 100×100 and 150×150 pixels to better match the reality. Finally, given the fact that the intensities of noise pixels in real CRs are subject to variation, we generate noise intensities from a truncated Gaussian distribution so the noise intensities will fall between 0 and 255; also, a standard deviation around 15 is used in the truncated normal distribution, which is close to the maximum standard deviation found in the 38 real samples. We then evaluate the performances of the DHR-RP method and the 5 other algorithms by calculating the average misclassification errors over each 1000 simulated images that have the same number of CRs. The evaluation results are summarized in Table 3. As suggested in Table 3, the DHR-RP algorithm clearly has the best performance for all the cases. More specifically, the MEs of the DHR-RP algorithm range from 2.2% to 6.21% for CR=1 and CR=15, respectively; however, the MEs of the second best algorithm (Bernsen's method) is 19%~74% larger than DHR-RP's. Also, the DHR-RP algorithm has the highest DCs for all cases (ranging from 0.35 to 0.70), which are at least 20% larger than those of the second best algorithm (Bernsen's method). Furthermore, the FPRs of our algorithm are the smallest among all methods in comparison. Although the FNRs of DHR-RP are not the smallest, no algorithms can achieve the smallest FRPs and FNRs simultaneously. Therefore, according to MEs and DCs of the algorithms under comparison, the DHR-RP method has the overall best performance.

We also realize that different image samples may have different features, which could affect algorithm performance. Therefore, we conduct additional simulation studies based on six different real image samples (see Fig. 12). The six samples are chosen for their different characteristics. That is, low vs. high vessel density in Fig. 12(a) and 12(b), respectively; low vs. high vessel curvature in Fig. 12(c) and 12(d), respectively; and low vs. high branch node density in Fig. 12(e) and 12(f), respectively. Based on each of the six real samples, 100 simulated images are generated by adding 15 CRs (contamination regions). Algorithm performances are evaluated again using ME, FPR, FNR and DC as in Table 4. The results clearly suggest that the DHR-RP method has the best performance in terms of MEs and DCs. The FPR of the DHR-RP algorithm is also the smallest for almost all the cases. As discussed before, although the FNRs of the DHR-RP algorithm are not the smallest, the MEs and DCs of this algorithm are convincing evidence of its overall superior performance over others. Finally, the histograms of ME, sensitivity, specificity and DC of the DHR-RP algorithm are plotted for visualization of their distributions as in Fig. 7 of the Supplementary Materials.

4.1.5 3D image example—Finally, to illustrate the performance of the DHR-RP method on 3D images, we conduct further experiments on 8 two-photon 3D vessel images. The RDH-RP method obtained satisfactory binarization results for all these real samples. However, limited by space, here we only show one thresholding result. Fig. 12(a) is the original image; in Figures 13(b) and 13(c), two different sets of low and high thresholds are used, respectively. The results in Figures 13(b) and (c) clearly suggest that the contaminated region can be appropriately removed, and the vessels in the original image have also been well preserved for both cases. In summary, the DHR-RP method is also naturally applicable to 3D image thresholding as we expect.

4.2. Tuning parameters

Several parameters need to be specified to use the DHR-RP method, which include the size of the sub-image window, the d-neighbor distance and the number of random probes. However, in practice, the only parameter that the DHR-RP method might be sensitive to is the size of the sub-window. We thus conducted further experiments and the results suggest that the performance of the algorithm is not sensitive to the change of the sub-window size (see supplementary Fig. 2 and Table 1 for details). Specifically in this study, we use a sub-window of 150×150 pixels for (1280×1024, 1031×825 and 1063×836) 2D images and a window of 30×30×30 for (220×220×110) 3D cases. Typical values of the d-neighbor distance could be from 5 to ≤30, depending on the image resolution as well as the size of objects in the image; in this study, we use a distance of 20 pixels for 2D cases and 5 voxels for 3D cases, respectively. As mentioned before, the larger the number of random probes for each sub-window, the better the performance; however, to reduce the computing cost, 100 probes usually will be sufficient to sample a sub-window.

Another issue that deserves further discussion is the scenarios in which the DHR-RP algorithm may fail. For example, if a random probe happens to fall at the center of a tube ring and the distance d happens to be the value such that all the d-neighbors fall on the ring, the frequencies of all the directional histogram bins will be equal to each other. Thus, even if the background is clean and there exist only tube-like objects in an image, the DHR will become 1 instead of being greater than 2. This is why we need to assume that "the spatial distribution of these objects is not isotropic with respect to all the directions used to generate the directional histogram" in Proposition 1. However, in practice, such scenarios are unlikely to occur because real vessels do not spread regularly in space. Furthermore, dividing the whole image into sub-windows can alleviate this problem because, e.g., a portion of a tube ring will lose the symmetry of the whole ring.

Finally, it should be addressed that the performance of the DHR-RP algorithm can be further improved. For example, a different threshold for binarization can be calculated for each different sub-window. Also, instead of sampling only one d-neighbor along each different direction at a random probe, one can sample multiple d-neighbors to generate a directional histogram at each random probe; in this way, the DHR will not be affected by the spatial orientation of a tube-like object and thus become more sensitive to the existence of tube-like objects. However, since our current implementation of the DHR-RP algorithm can already achieve superior performance, we leave the investigation of possible variations of the DHR-RP algorithm to the future.

4.3. Computational complexity

For the proposed DHR-RP algorithm, mainly the multi-level Otsu method and the calculation of DH cost more computing time. The computational complexity of multi-level Otsu has been analyzed in [66] and [85], thus in this paper we will only discuss the computational cost of the DH calculation. Use the same notations as in section III, we assume there are $w_{\max}$ sub-windows in the computed image and we plant n random probes within each sub-image to calculate the DH. In the worst case (that is, every neighbor pixel checked needs to be added to the DH), there will be $8w_{\max}n$ of additions for 2D cases and $26w_{\max}n$ additions for 3D cases. Besides these additions, the maximum and minimum of the 8 or 26 dimensions of DH vector should be searched with a complexity of $O(8)$ or $O(26)$. One extra division is needed for each sub-window to calculate the DHR, which would require $w_{\max}$ of divisions for the whole image. Therefore, the computational complexity of DHR-RP is linearly proportional to $w_{\max}n$ without considering the multi-level Otsu part, which is totally acceptable for the thresholding need.

5. Conclusion

In this study, we developed a novel algorithm for capillary image thresholding. In particular, the proposed method, called directional histogram ratio at random probes (DHR-RP), explicitly takes the geometric feature of vessels into consideration and to our best knowledge, this idea is proposed for the very first time. Specifically, within each sub-window of either a 2D or 3D image, a number of random probes are planted on bright pixels/voxels to collect their so-called *d*-neighbors along multiple different directions; then a directional histogram is generated based on the intensities of these *d*-neighbors and the ratio of the maximum and minimum bin frequencies of the histogram is calculated as an indicator of the existence of tube-like objects as well as the severity of contamination. A low DHR (<2) indicates a heavily contaminated region and thus one can choose a high threshold for image binarization; contrarily, a large ratio ($\gg 2$) suggests the use of a low threshold for binarization. We then theoretically and experimentally verified the performance of the DHR-RP. The results suggest that the DHR-RP approach outperforms many existing algorithms under a number of different conditions (i.e., different numbers, sizes and noise intensities of contamination regions). We also illustrated that the DHR-RP algorithm is applicable to both 2D and 3D vessel images. We also realize that the DHR-RP method is specialized to images with tube-like objects; however, in the future, this method can be extended to images with objects of different shapes by changing, e.g., the way how the random probes sample their neighbors.

Supplementary Material

Refer to Web version on PubMed Central for supplementary material.

Acknowledgments

This work is supported in part by NIH/NIAID grants P30AI078498, HHSN272201000055C, PO1MH64570, R01DA026325, T32GM007356 (J.S.) as well as the National Natural Foundation of China grant 61105034, Research Fund for the Doctoral Program of Higher Education of China grant 20100201120040, China Postdoctoral Science Foundation grant 20110491662, 2012T50805. We gratefully acknowledge Linda Callahan and the URMC Two Photon Core facility for assistance with two-photon imaging studies.

References

1. Kasischke KA, Lambert EM, Panepento B, Sun A, Gelbard HA, Burgess RW, Foster TH, Nedergaard M. Two-photon NADH imaging exposes boundaries of oxygen diffusion in cortical vascular supply regions. J Cereb Blood Flow Metab. 2011; 31:68–81. [PubMed: 20859293]
2. Polesskaya O, Silva J, Sanfilippo C, Desrosiers T, Sun A, Shen J, Feng C, Polesskiy A, Deane R, Zlokovic B, Kasischke K, Dewhurst S. Methamphetamine causes sustained depression in cerebral blood flow. Brain Research. 2011; 1373:91–100. [PubMed: 21156163]
3. Gerber SA, Moran JP, Frelinger JG, Frelinger JA, Fenton BM, Lord EM. Mechanism of IL-12 mediated alterations in tumour blood vessel morphology: analysis using whole-tissue mounts. Br J Cancer. 2003; 88:1453–1461. [PubMed: 12778077]
4. Gerber SA, Rybalko VY, Bigelow CE, Lugade AA, Foster TH, Frelinger JG, Lord EM. Preferential Attachment of Peritoneal Tumor Metastases to Omental Immune Aggregates and Possible Role of a Unique Vascular Microenvironment in Metastatic Survival and Growth. The American Journal of Pathology. 2006; 169:1739–1752. [PubMed: 17071597]
5. Suárez Y, Fernández-Hernando C, Yu J, Gerber SA, Harrison KD, Pober JS, Iruela-Arispe ML, Merkenschlager M, Sessa WC. Dicer-dependent endothelial microRNAs are necessary for postnatal angiogenesis. Proceedings of the National Academy of Sciences. 2008; 105:14082–14087.
6. Denk W, Svoboda K. Photon Upmanship: Why Multiphoton Imaging Is More than a Gimmick. Neuron. 1997; 18:351–357. [PubMed: 9115730]

7. Denk W, Strickler J, Webb W. Two-photon laser scanning fluorescence microscopy. Science. 1990; 248:73–76. [PubMed: 2321027]

8. Parsons-Wingerter P, Lwai B, Yang MC, Elliott KE, Milaninia A, Redlitz A, Clark JI, Sage EH. A Novel Assay of Angiogenesis in the Quail Chorioallantoic Membrane: Stimulation by bFGF and Inhibition by Angiostatin According to Fractal Dimension and Grid Intersection. Microvascular Research. 1998; 55:201–214. [PubMed: 9657920]

9. Blacher S, Devy L, Hlushchuk R, Larger E, Lamandé N, Burri P, Corvol P, Djonov V, Foidart J-M, Noël A. Quantification of angiogenesis in the chiken chorioallantoic membrane (CAM). Image Analysis & Stereology. 2005; 24:169–180.

10. Doukas CN, Maglogiannis I, Chatziioannou AA. Computer-Supported Angiogenesis Quantification Using Image Analysis and Statistical Averaging, Information Technology in Biomedicine. IEEE Transactions on. 2008; 12:650–657.

11. Pyriochou A, Tsigkos S, Vassilakopoulos T, Cottin T, Zhou Z, Gourzoulidou E, Roussos C, Waldmann H, Giannis A, Papapetropoulos A. Anti-angiogenic properties of a sulindac analogue. British Journal of Pharmacology. 2007; 152:1207–1214. [PubMed: 17965739]

12. Strick DM, Waycaster RL, Montani JP, Gay WJ, Adair TH. Morphometric measurements of chorioallantoic membrane vascularity: effects of hypoxia and hyperoxia. American Journal of Physiology - Heart and Circulatory Physiology. 1991; 260:H1385–H1389.

13. Larger E, Marre M, Corvol P, Gasc J-M. Hyperglycemia-Induced Defects in Angiogenesis in the Chicken Chorioallantoic Membrane Model. Diabetes. 2004; 53:752–761. [PubMed: 14988261]

14. Wei, D-m; Gao, Y.; Cao, X-r; Zhu, N-c; Liang, J-f; Xie, W-p; Zhen, M-y; Zhu, M-s. Soluble multimer of recombinant endostatin expressed in E. coli has anti-angiogenesis activity. Biochemical and Biophysical Research Communications. 2006; 345:1398–1404. [PubMed: 16723120]

15. Cassot F, Lauwers F, Fouard C, Prohaska S, Lauwers-Cances V. A Novel Three-Dimensional Computer-Assisted Method for a Quantitative Study of Microvascular Networks of the Human Cerebral Cortex. Microcirculation. 2006; 13:1–18. [PubMed: 16393942]

16. Di Ieva A, Grizzi F, Ceva-Grimaldi G, Russo C, Gaetani P, Aimar E, Levi D, Pisano P, Tancioni F, Nicola G, Tschabitscher M, Dioguardi N, Baena RRy. Fractal dimension as a quantitator of the microvasculature of normal and adenomatous pituitary tissue. Journal of Anatomy. 2007; 211:673–680. [PubMed: 17784937]

17. Lauwers F, Cassot F, Lauwers-Cances V, Puwanarajah P, Duvernoy H. Morphometry of the human cerebral cortex microcirculation: General characteristics and space-related profiles. NeuroImage. 2008; 39:936–948. [PubMed: 17997329]

18. Risser L, Plouraboue F, Steyer A, Cloetens P, Le Duc G, Fonta C. From homogeneous to fractal normal and tumorous microvascular networks in the brain. J Cereb Blood Flow Metab. 2006; 27:293–303. [PubMed: 16736048]

19. Kirbas C, Quek F. A review of vessel extraction techniques and algorithms. ACM Comput Surv. 2004; 36:81–121.

20. Lesage D, Angelini ED, Bloch I, Funka-Lea G. A review of 3D vessel lumen segmentation techniques: Models, features and extraction schemes. Medical Image Analysis. 2009; 13:819–845. [PubMed: 19818675]

21. Tsai PS, Kaufhold JP, Blinder P, Friedman B, Drew PJ, Karten HJ, Lyden PD, Kleinfeld D. Correlations of neuronal and microvascular densities in murine cortex revealed by direct counting and colocalization of nuclei and vessels. The Journal of Neuroscience. 2009; 29:14553–14570. [PubMed: 19923289]

22. Risser L, Plouraboue F, Descombes X. Gap Filling of 3-D Microvascular Networks by Tensor Voting, Medical Imaging. IEEE Transactions on. 2008; 27:674–687.

23. Risser L, Plouraboué F, Cloetens P, Fonta C. A 3D-investigation shows that angiogenesis in primate cerebral cortex mainly occurs at capillary level. International Journal of Developmental Neuroscience. 2009; 27:185–196. [PubMed: 19038323]

24. Socher R, Barbu A, Comaniciu D. A learning based hierarchical model for vessel segmentation. Proc IEEE Int Symp Biomed Imaging. 2008:1055–1058.

25. Xue J-H, Titterington DM. Median-based image thresholding. Image and Vision Computing. 2011; 29:631–637.
26. van Aarle W, Batenburg KJ, Sijbers J. Optimal Threshold Selection for Segmentation of Dense Homogeneous Objects in Tomographic Reconstructions, Medical Imaging. IEEE Transactions on. 2011; 30:980–989.
27. Ming-Huwi H. A multilevel image thresholding using the honey bee mating optimization. Applied Mathematics and Computation. 2010; 215:3302–3310.
28. Chen Q, Sun Q-s, Heng PA, Xia D-s. A double-threshold image binarization method based on edge detector. Pattern Recogn. 2008; 41:1254–1267.
29. Condurache, TAAP. Vessel segmentation in angiograms using hysteresis thresholding. IAPR Conference on Machine Vision Applications Tsukuba; Japan. 2005. p. 269-272.
30. Batenburg KJ, Sijbers J. Optimal Threshold Selection for Tomogram Segmentation by Projection Distance Minimization, Medical Imaging. IEEE Transactions on. 2009; 28:676–686.
31. Doyle W. Operations Useful for Similarity-Invariant Pattern Recognition. J ACM. 1962; 9:259–267.
32. Sezgin M, Sankur Bl. Survey over image thresholding techniques and quantitative performance evaluation. Journal of Electronic Imaging. 2004; 13:146–168.
33. Rosenfeld A, Torre PDl. Histogram concavity analysis as an aid in threshold selection IEEE Transaction on Systems. Man and Cybernetics. 1983; SMC-13:231–235.
34. Sahasrabudhe SC, Gupta KSD. A valley-seeking threshold selection technique. Computer Vision and Image Understanding. 1992; 56:55–65.
35. Guo R, Pandit SM. Automatic threshold selection based on histogram modes and a discriminant criterion. Mach Vision Appl. 1998; 10:331–338.
36. Carlotto MJ. Histogram Analysis Using a Scale-Space Approach, Pattern Analysis and Machine Intelligence. IEEE Transactions on. 1987; PAMI-9:121–129.
37. Du-Ming T. A fast thresholding selection procedure for multimodal and unimodal histograms. Pattern Recognition Letters. 1995; 16:653–666.
38. Otsu N. A Threshold Selection Method from Gray-Level Histograms, Systems, Man and Cybernetics. IEEE Transactions on. 1979; 9:62–66.
39. Bazi Y, Bruzzone L, Melgani F. Image thresholding based on the EM algorithm and the generalized Gaussian distribution. Pattern Recognition. 2007; 40:619–634.
40. Kittler J, Illingworth J. On threshold selection using clustering criteria, IEEE Transaction on Systems. Man and Cybernetics. 1985; SMC-15:652–655.
41. Kittler J, Illingworth J. Minimum error thresholding. Pattern Recogn. 1986; 19:41–47.
42. Cho S, Haralick R, Yi S. Improvement of Kittler and Illingworth's minimum error thresholding. Pattern Recogn. 1989; 22:609–617.
43. Chang C-I, Chen K, Wang J, Althouse MLG. A relative entropy-based approach to image thresholding. Pattern Recognition. 1994; 27:1275–1289.
44. Li CH, Lee CK. Minimum cross entropy thresholding. Pattern Recognition. 1993; 26:617–625.
45. Jui-Cheng Y, Fu-Juay C, Shyang C. A new criterion for automatic multilevel thresholding, Image Processing. IEEE Transactions on. 1995; 4:370–378.
46. Pun T. Entropic thresholding: A new approach. Computer Graphics and Image Processing. 1981; 16:210–239.
47. Cheng HD, Cheng Y-H, Sun Y. A novel fuzzy entropy approach to image enhancement and thresholding. Signal Process. 1999; 75:277–301.
48. Sahoo P, Wilkins C, Yeager J. Threshold selection using Renyi's entropy. Pattern Recognition. 1997; 30:71–84.
49. Pikaz A, Averbuch A. Digital image thresholding, based on topological stable-state. Pattern Recogn. 1996; 29:829–843.
50. Ramar K, Arumugam S, Sivanandam SN, Ganesan L, Manimegalai D. Quantitative fuzzy measures for threshold selection. Pattern Recogn Lett. 2000; 21:1–7.
51. O'Gorman L. Binarization and multithresholding of document images using connectivity. CVGIP: Graph Models Image Process. 1994; 56:494–506.

52. A Note on the Use of (Gray Level, Local Average Gray Level) Space as an Aid in Threshold Selection, Systems, Man and Cybernetics. IEEE Transactions on. 1979; 9:860–864.
53. Rosenfeld A, Smith RC. Thresholding Using Relaxation, Pattern Analysis and Machine Intelligence. IEEE Transactions on. 1981; PAMI-3:598–606.
54. Wu AY, Hong T-H, Rosenfeld A. Threshold Selection Using Quadtrees, Pattern Analysis and Machine Intelligence. IEEE Transactions on. 1982; PAMI-4:90–94.
55. A Note on the Use of Second-Order Gray-Level Statistics for Threshold Selection, Systems, Man and Cybernetics. IEEE Transactions on. 1978; 8:895–898.
56. Lie W-N. An efficient threshold-evaluation algorithm for image segmentation based on spatial graylevel co-occurrences. Signal Process. 1993; 33:121–126.
57. Putra, SPAR.; Sim Chong, K.; Abdullah, K.; Lim Hwee, S.; Nordin, MNM. Texture analysis of AIRSAR images for land cover classification, Space Science and Communication (IconSpace). 2011 IEEE International Conference; 2011; p. 243-248.
58. Li CH, Tam PKS. An iterative algorithm for minimum cross entropy thresholding. Pattern Recognition Letters. 1998; 19:771–776.
59. Febriiliyan Samopa AA. Hybrid image thresholding method using edge detection. International Journal of Computer Science and Network Security. 2009; 9:292–299.
60. Venkateswarlu NB, Boyle RD. New Segmentation Techniques for Document Image Analysis. Image and Vision Computing. 1995; 13:573–583.
61. Wonho O, Lindquist B. Image thresholding by indicator kriging, Pattern Analysis and Machine Intelligence. IEEE Transactions on. 1999; 21:590–602.
62. Yan F, Zhang H, Kube CR. A multistage adaptive thresholding method. Pattern Recognition Letters. 2005; 26:1183–1191.
63. Huang K, Wang M-JJ. Image thresholding by minimizing the measures of fuzziness. Pattern Recognition. 1995; 28:41–51.
64. Yuksel ME, Borlu M. Accurate Segmentation of Dermoscopic Images by Image Thresholding Based on Type-2 Fuzzy Logic, Fuzzy Systems. IEEE Transactions on. 2009; 17:976–982.
65. Fan S-KS, Lin Y. A multi-level thresholding approach using a hybrid optimal estimation algorithm. Pattern Recognition Letters. 2007; 28:662–669.
66. Liao P-S, Chen T-S, Chung P-C. A Fast Algorithm for Multilevel Thresholding. Journal of Information Science and Engineering. 2001; 17:713–727.
67. Nowak-Sliwinska P, Ballini J-P, Wagnières G, van den Bergh H. Processing of fluorescence angiograms for the quantification of vascular effects induced by anti-angiogenic agents in the CAM model. Microvascular Research. 2010; 79:21–28. [PubMed: 19857502]
68. Kirbas, C.; Quek, FKH. Vessel extraction techniques and algorithms: a survey, Bioinformatics and Bioengineering, 2003. Proceedings. Third IEEE Symposium; 2003; p. 238-245.
69. Hoover AD, Kouznetsova V, Goldbaum M. Locating blood vessels in retinal images by piecewise threshold probing of a matched filter response, Medical Imaging. IEEE Transactions on. 2000; 19:203–210.
70. Xu, F.; Wang, X-c; Zhou, M-q; Wu, Z.; Liu, X-y. Segmentation algorithm of brain vessel image based on SEM statistical mixture model, Fuzzy Systems and Knowledge Discovery (FSKD). 2010 Seventh International Conference; 2010; p. 1830-1833.
71. Fabijanska, A. A survey of thresholding algorithms on yarn images, Perspective Technologies and Methods in MEMS Design (MEMSTECH). 2010 Proceedings of VIth International Conference; 2010; p. 23-26.
72. Ojala T, Pietikäinen M, Harwood D. A comparative study of texture measures with classification based on featured distributions. Pattern Recognition. 1996; 29:51–59.
73. Akif Gulsun, HTM. Proceedings of the 11th international conference on Medical Image Computing and Computer-Assisted Intervention - Part I. Springer-Verlag; New York, NY, USA: 2008. Robust Vessel Tree Modeling; p. 602-611.
74. Wesarg, S.; Firle, E. Segmentation of vessels: the corkscrew algorithm. In: Fitzpatrick, M.; Sonka, M., editors. Medical Imaging Symposium, SPIE. 2004. p. 1609-1620.

75. Xinguo, L.; Su, R.; Sing Bing, K.; Heung-Yeung, S. Directional histogram model for three-dimensional shape similarity, Computer Vision and Pattern Recognition, 2003. Proceedings. 2003 IEEE Computer Society Conference; 2003. p. I-813-I-820.
76. Brown, EB.; Webb, WW. Two-photon activation of caged calcium with submicron, submillisecond resolution. In: Gerard, M., editor. Methods in Enzymology. Academic Press; 1998. p. 356-380.
77. Whitmore, RL. Rheology of the Circulation. Pergamon Press; Oxford: 1968.
78. Kapur JN, Sahoo PK, Wong AKC. A new method for gray-level picture thresholding using the entropy of the histogram. Computer Vision, Graphics, and Image Processing. 1985; 29:273–285.
79. Zack GW, Rogers WE, Latt SA. Automatic measurement of sister chromatid exchange frequency. Journal of Histochemistry & Cytochemistry. 1977; 25:741–753. [PubMed: 70454]
80. Bernsen, J. Dynamic thresholding of gray-level images. International Conference on Pattern Recognition; Paris, France. 1986. p. 1251-1255.
81. Gonzales, RWR. Digital image processing. Addison-Wesley Publishing Company; 1992.
82. Niblack, W. An introduction to digital image processing. Prentice-Hall; 1986.
83. Sauvola J, Pietikäinen M. Adaptive document image binarization. Pattern Recognition. 2000; 33:225–236.
84. Dice LR. Measures of the Amount of Ecologic Association Between Species. Ecology. 1945; 26:297–302.
85. Gong J, Li L, Chen W. Fast recursive algorithms for two-dimensional thresholding. Pattern Recognition. 1998; 31:295–300.

Biographies

Na Lu received her B.S. and Ph.D. degrees from Xi'an Jiaotong University, Xi'an, Shaanxi, China in 2002 and 2008, respectively. She studied in the State Key Laboratory of Manufacturing Systems Engineering, Systems Engineering Institute, Xi'an Jiaotong University, Xi'an, Shaanxi, China. Currently, she is an Assistant Professor at Xi'an Jiaotong University, Xi'an, Shaanxi, China. Her research interests include image processing, image analysis, pattern recognition and robotics.

Jharon Silva is a Ph.D. student at the Department of Microbiology and Immunology, University of Rochester, Rochester, NY. His research focuses on HIV-related two-photon vessel imaging.

Yu Gu received her M.S. degree from the Department of Electric and Computer Engineering at University of Rochester in 2010. She specializes in image processing and computing.

Scott Gerber is a Ph.D. student at the Department of Microbiology and Immunology, University of Rochester, Rochester, NY. His research focuses on whole-mount imaging.

Hulin Wu received his Ph.D. from the Department of Statistics, Florida State University, Florida in 1994. He is Professor of the Department of Biostatistics & Computational Biology, Professor of the Department of Medicine, and Professor of the Department of Community and Preventative Medicine at University of Rochester. He is an expert in mathematical modeling and statistical analysis of biomedical data, including images.

Harris Gelbard received his M.D. and Ph.D. degrees from Northwestern University in 1983. He is currently Professor of the Department of Neurology and Professor of the Department of Microbiology & Immunology, University of Rochester, Rochester, NY. He has 25 years of experience as a molecular neuropharmacologist, working in experimental models of neuroAIDS and HIV-1 neuroinflammation using various imaging techniques.

Stephen Dewhurst received his B.S. degree from Bristol University, UK in 1984 and his Ph.D. degree from University of Nebraska, USA in 1987. He performed postdoctoral training at Columbia University and at the Harvard School of Public Health. He is currently Dean's Professor and Chair of Microbiology & Immunology at the University of Rochester School of Medicine and Dentistry (URSMD). His research work focused on the pathogenesis of human and simian immunodeficiency viruses, including using imaging techniques to understand vascular responses.

Hongyu Miao received his M.S. in Biostatistics and Ph.D. degrees in Mechanical Engineering from University of Rochester, Rochester, NY in 2011 and 2007, respectively. He is currently Assistant Professor of the Department of Biostatistics & Computational Biology, University of Rochester, Rochester, NY. His research interests include mathematical modeling, statistical image analysis, computational biology, systems biology and infectious diseases.

- Thresholding algorithm deals with both clean and heavily contaminated vessel images
- Random probes sample the geometric features of tube-like objects
- Directional histogram ratio can be an indicator of both contamination and existence of tube objects
- DHR-RP has a superior performance over existing approaches based on real samples and an extensive simulation study

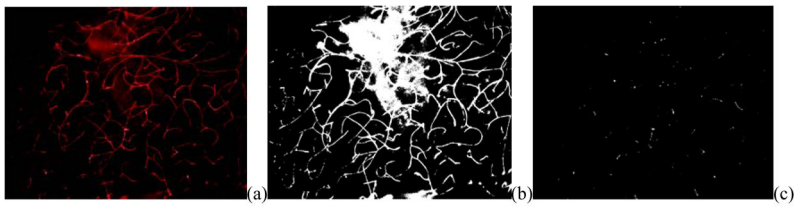

Fig 1.

Illustration of the contamination problem in two-photon vessel image. (a) Two photon vessel image; (b) Thresholding result of the Kittler's method; (c) Thresholding result of the maximum entropy method.

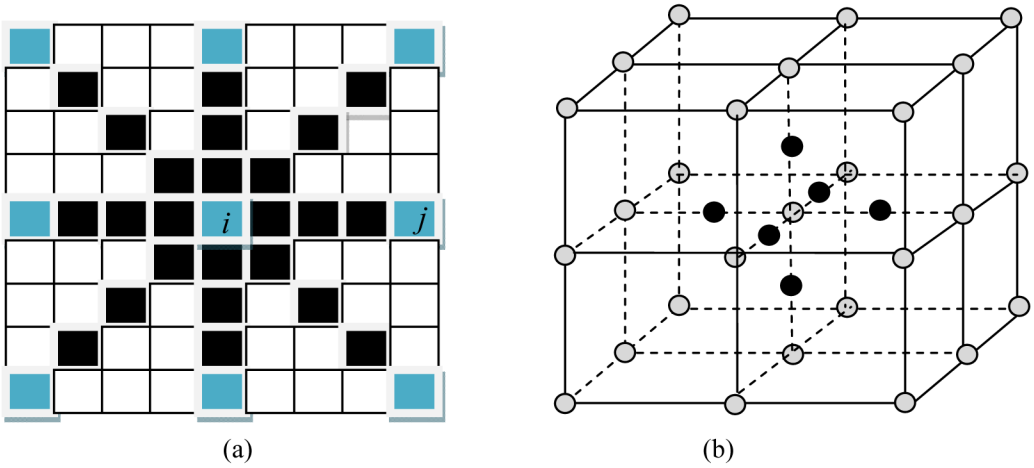

Fig 2.

Schematic illustration of d-neighbors in multiple different directions. (a) A 2D case where the light pixel at the center is a randomly selected pixel and the eight light pixels on the border are its 3-neighbors. (b) A 3D case where the light sphere at the center of the cube is a randomly selected voxel and the light spheres on the surfaces are its 1-neighbors (only six black spheres in between light spheres are shown here for a clear view).

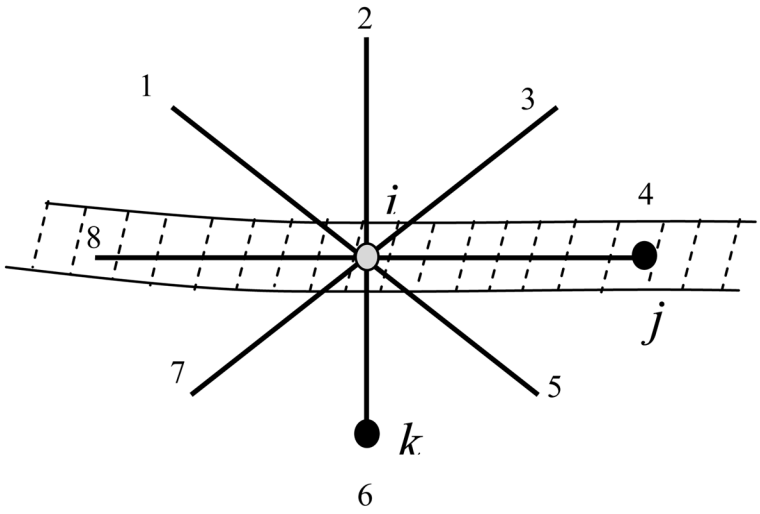

Fig 3.

Illustration of a tube-like object using an 8-directional probe. The shadowed part is an object. Pixel *i* is a randomly selected pixel on the object and *j* and *k* are two *d*-neighbors of *i*.

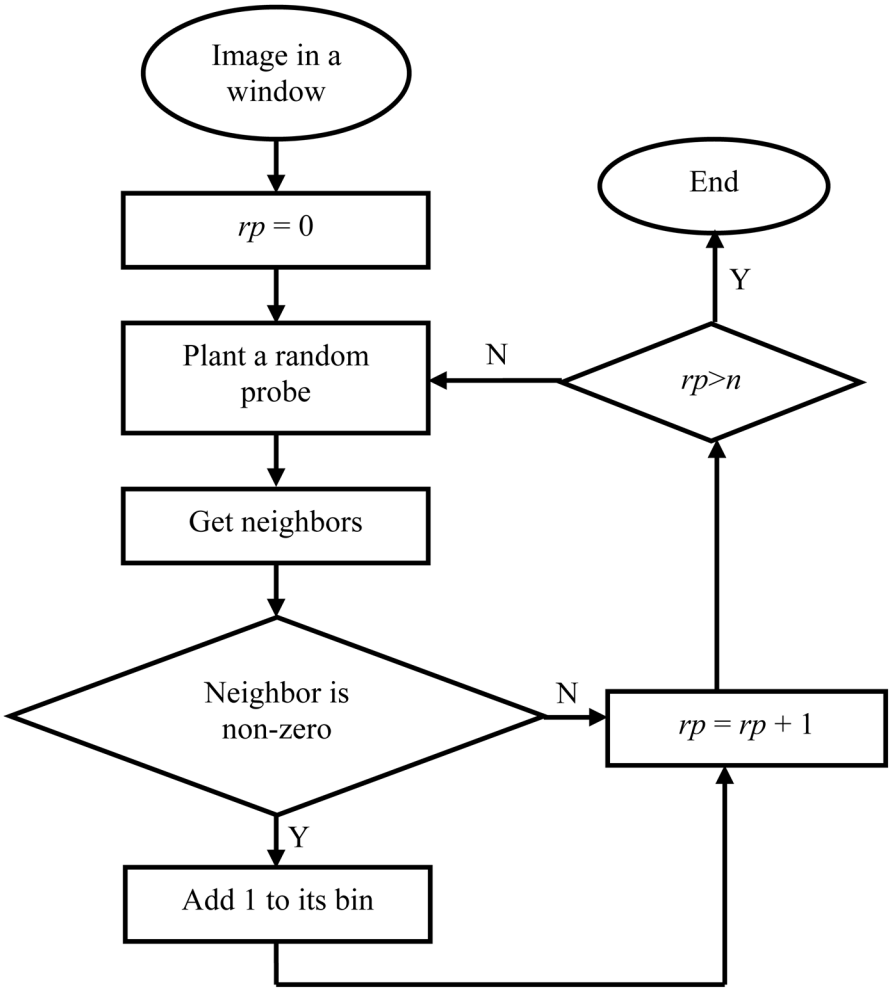

Fig 4.
Flow chart for generating the directional histogram.

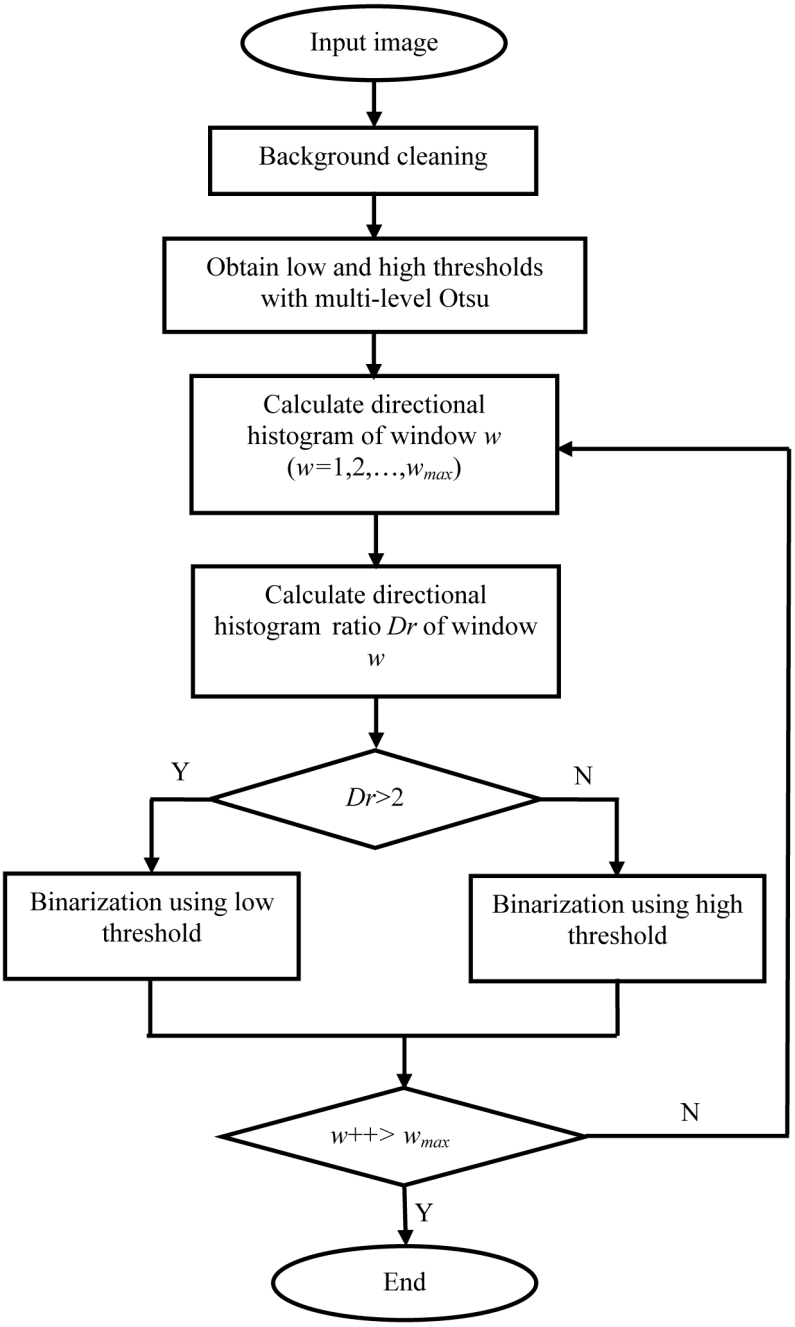

Fig 5.
Flow chart of the DHR-RP thresholding algorithm.

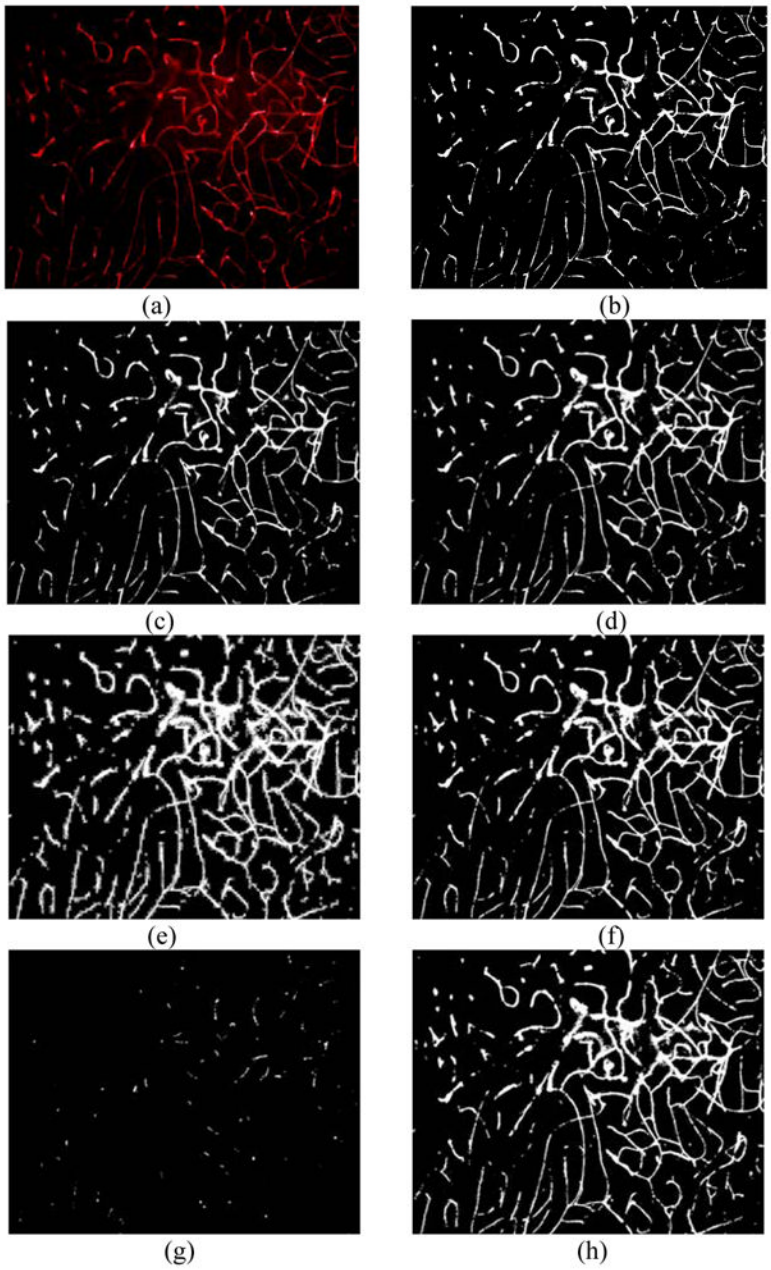

Fig 6.

Results of seven different thresholding methods applied to a high-quality two-photon vessel image. (a) Original image. (b) DHR-RP method. (c) Otsu method. (d) Huang's method. (e) Percentile method. (f) Triangle method. (g) Maximum entropy method. (h) Kittler's method.

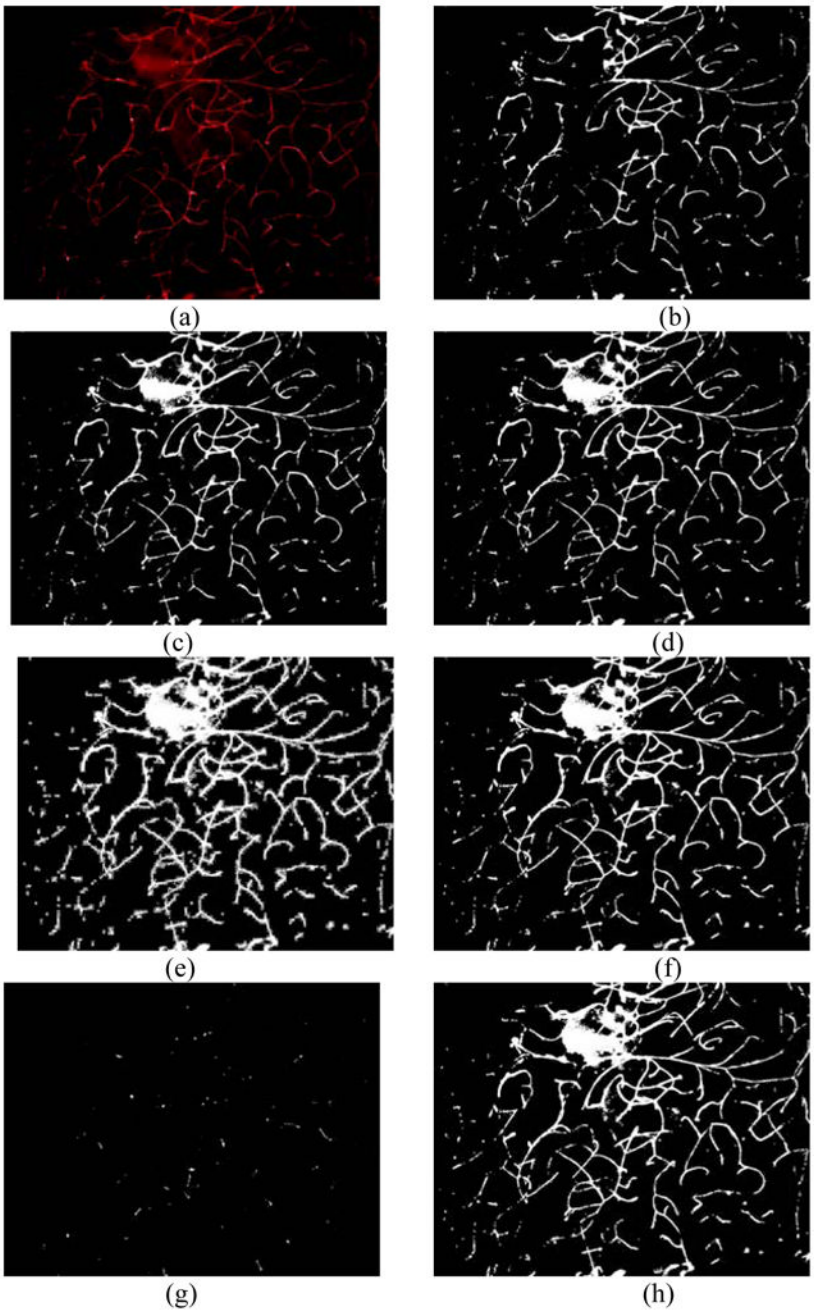

Fig 7.

Results of seven different thresholding methods applied to a moderately contaminated two-photon vessel image. (a) Original image. (b) DHR-RP method. (c) Otsu method. (d) Huang's method. (e) Percentile method. (f) Triangle method. (g) Maximum entropy method. (h) Kittler's method.

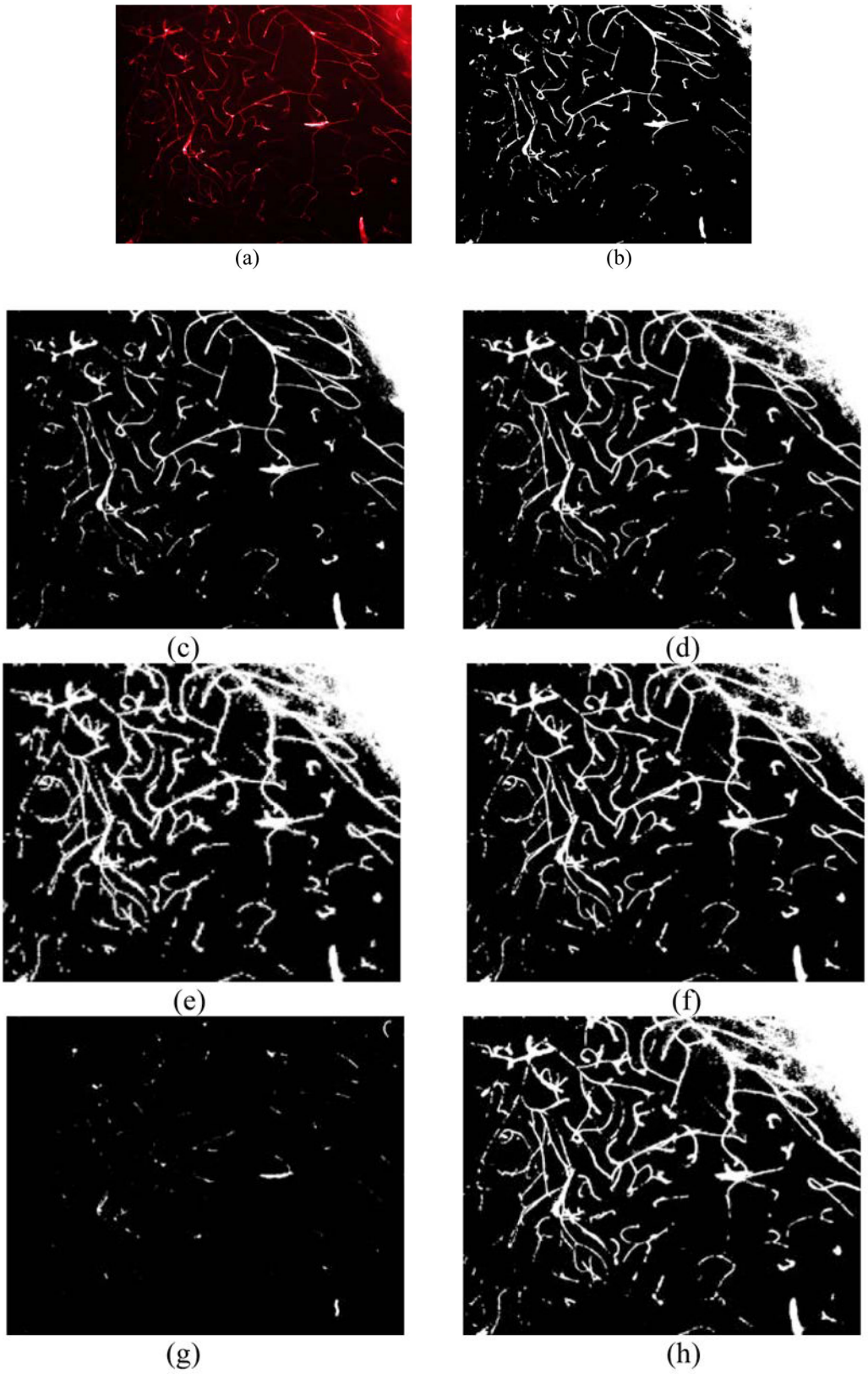

Fig 8.

Results of seven different thresholding methods applied to a heavily contaminated two-photon vessel image. (a) Original image. (b) DHR-RP method. (c) Otsu method. (d) Huang's method. (e) Percentile method. (f) Triangle method. (g) Maximum entropy method. (h) Kittler's method.

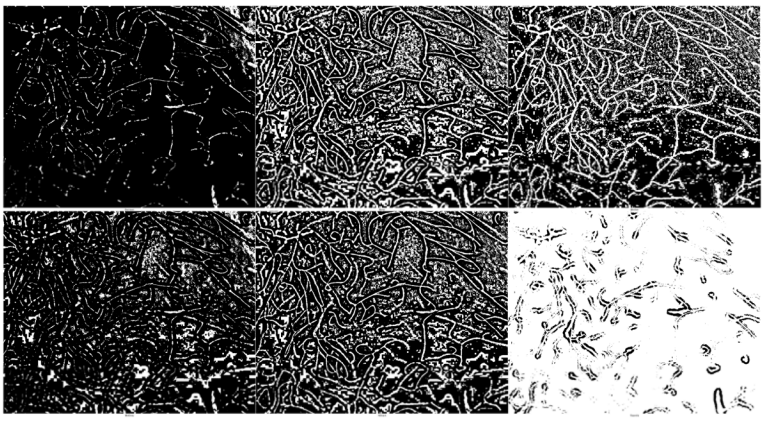

Fig 9.

Local thresholding results of the two-photon vessel image in Fig. 8(a). The open source software ImageJ is employed to obtain these results using the default computing parameters. The three images in the upper row are results of Bersen's method, the mean method and the median method. The three images in the lower row are results of MidGray's method, Niblack's method and Sauvola's method.

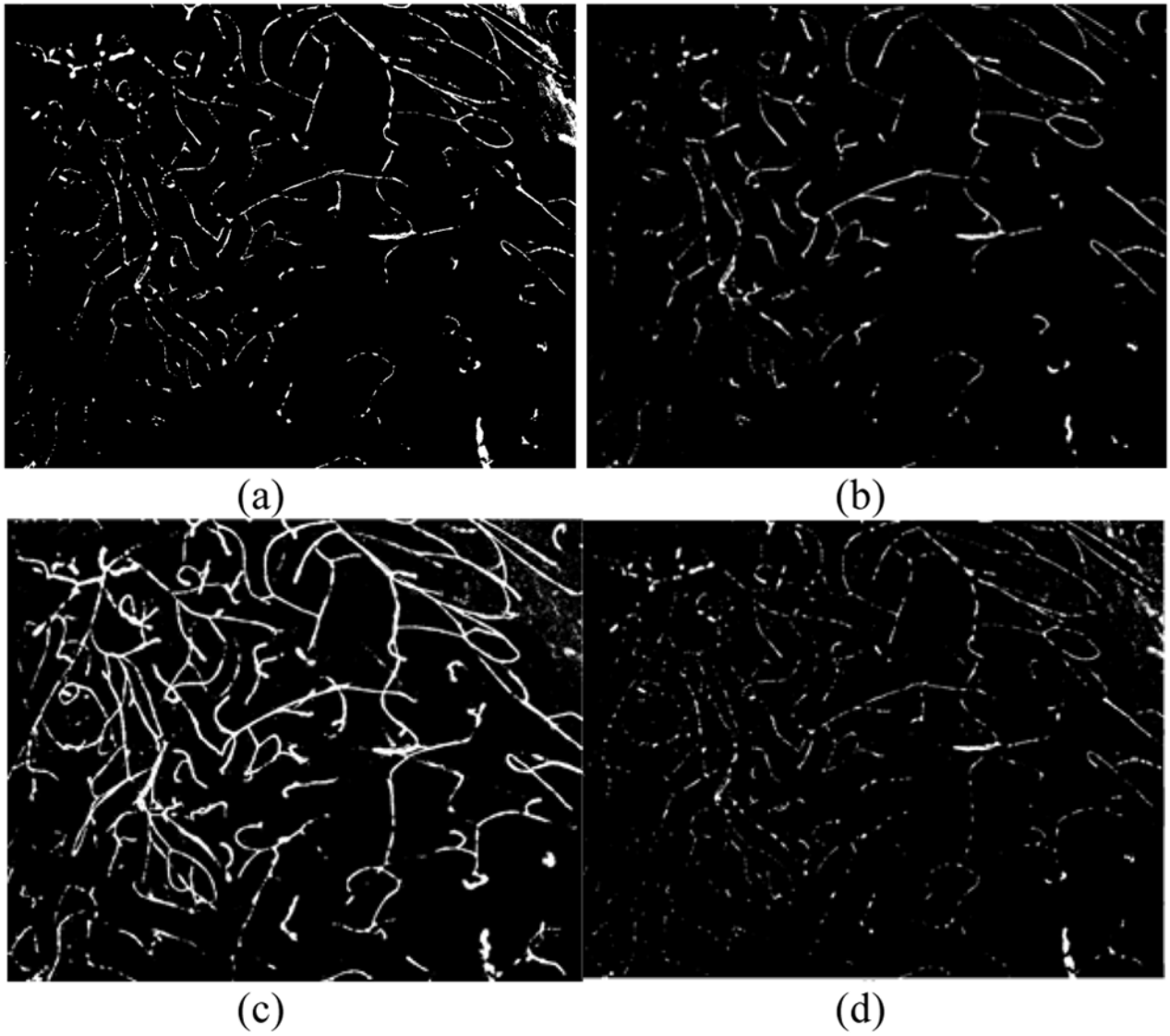

Fig 10.

Improved local thresholding results by finely tuning computing parameters. (a) Result of Bernsen's method. (b) Result of the mean method. (c) Result of the median method. (d) Result of the MidGray method.

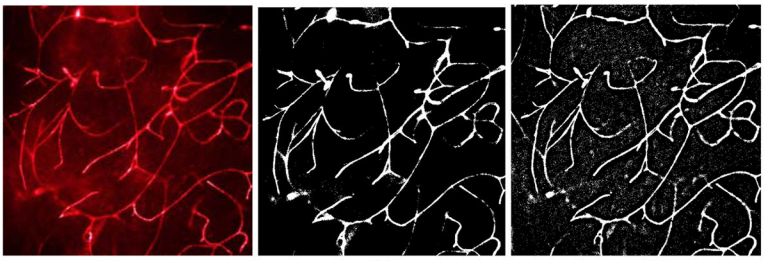

(a) (b) (c)

Fig 11.

Comparison of the DHR-RP method with the mean method. (a) Original image. (b) Result of the DHR-RP method. (c) Result of the mean method.

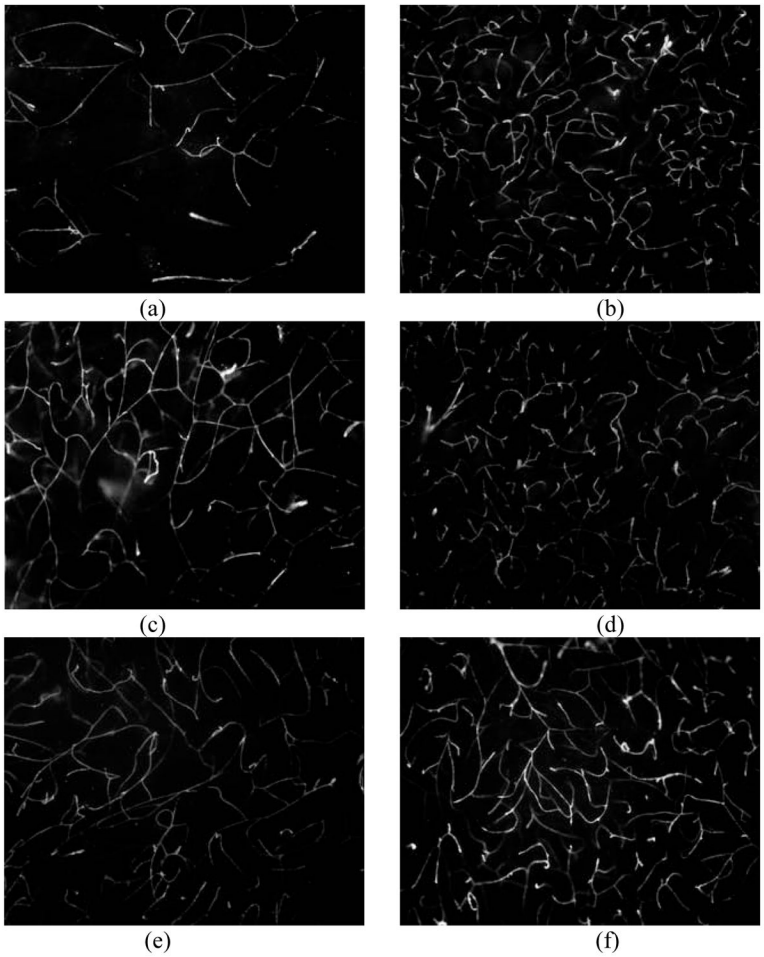

Figure 12.

Six real image samples with different features. (a) Low vessel density. (b) High vessel density. (c) Low vessel curvature. (d) High vessel curvature. (e) Low branch node density. (f) High branch node density.

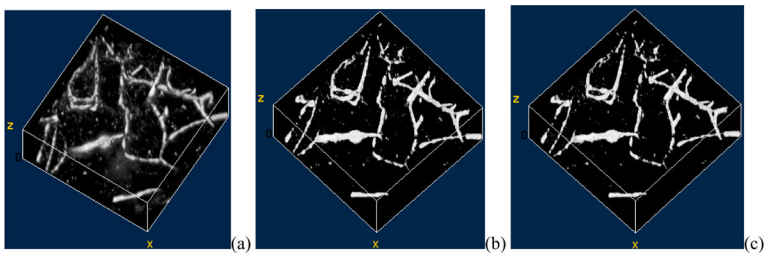

Fig 13.

Thresholding results of the DHR-RP algorithm on a 3D two-photon vessel image. (a) Original image. (b) DHR-RP thresholding result with a lower threshold. (c) DHR-RP thresholding result with a higher threshold.

Table 1

Summary of the representative thresholding methods.

Category	Feature	Applicability
Histogram based	Use intensity histogram shape; Conceptually simple;	Mostly for unimodal histograms or histograms with well-separated peaks;
Entropy based	Optimize (cross-)entropy; Many existing tools and theories for optimization problems;	Empirical; Using second-order entropy can usually lead to better performance;
Attribute based	Incorporate information from not only intensity but also edge, gray-level moments etc.	Images with low noise level; Accurate feature extraction methods are required;
Spatial distribution based	Consider spatial correlation; Flexible;	Need distribution assumption; Images of low noise level;
Clustering based	Use similarity or dissimilarity between foreground and background; Effective and broadly used;	Better performance for images with well-separated background and foreground;
Local statistics based	Use adaptive thresholds; Usually have a better performance than global approaches;	Subject to the choice of statistics; Images of low noise level;

Table 2

Quantitative comparison of algorithm performance based on Fig. 7(a).

Thresholding methods	DHR-RP	Ostu	Huang	Kittler	Maximum entropy	Local mean	Bernsen
ME (%)	2.48	2.78	3.06	5.06	5.82	4.16	4.23
FPR (%)	0.48	1.97	2.61	5.20	0.01	4.03	1.33
FNR (%)	34.11	15.60	10.14	2.91	97.64	6.12	49.97
DC	0.90	0.73	0.69	0.54	0.96	0.60	0.70

Table 3

Average ME, FPR, FNR, and DC of thresholding algorithms. CR denotes contamination region and the integer after CR denotes the number of regions added in the simulated images. Each 1000 image samples are generated for each different number of CRs, and the average misclassification error is calculated based on each 1000 images.

Method	Criterion	CR1	CR2	CR3	CR5	CR10	CR15
DHR-RP	**ME ± SD (%)**	**2.20 ± 0.25**	**2.58 ± 0.26**	**2.89 ± 0.36**	**3.49 ± 0.50**	**5.04 ± 0.76**	**6.21 ± 0.82**
	FPR ± SD (%)	**1.34 ± 0.30**	**1.70 ± 0.33**	**2.04 ± 0.43**	**2.55 ± 0.64**	**4.25 ± 0.92**	**5.43 ± 0.99**
	FNR ± SD (%)	23.84 ± 3.98	24.72 ± 4.59	24.58 ± 5.08	27.18 ± 7.25	25.15 ± 6.09	25.78 ± 6.05
	DC ± SD	**0.70 ± 0.04**	**0.64 ± 0.04**	**0.60 ± 0.05**	**0.54 ± 0.06**	**0.42 ± 0.05**	**0.35 ± 0.03**
Otsu	**ME ± SD (%)**	4.38 ± 0.24	4.91 ± 0.29	5.45 ± 0.40	6.49 ± 0.47	8.99 ± 0.74	11.19 ± 0.79
	FPR ± SD (%)	4.46 ± 0.25	5.01 ± 0.31	5.57 ± 0.42	6.65 ± 0.50	9.25 ± 0.77	11.53 ± 0.82
	FNR ± SD (%)	2.34 ± 0.15	2.37 ± 0.20	2.42 ± 0.23	2.48 ± 0.26	2.65 ± 0.28	2.70 ± 0.28
	DC ± SD	0.46 ± 0.01	0.44 ± 0.02	0.41 ± 0.02	0.37 ± 0.02	0.30 ± 0.02	0.25 ± 0.01
Huang	**ME ± SD (%)**	17.09 ± 0.46	17.78 ± 0.55	18.60 ± 0.69	19.97 ± 0.89	17.33 ± 3.74	17.51 ± 1.33
	FPR ± SD (%)	17.75 ± 0.48	18.47 ± 0.57	19.32 ± 0.72	20.73 ± 0.93	17.98 ± 3.90	18.16 ± 1.38
	FNR ± SD (%)	0.56 ± 0.01	0.56 ± 0.01	0.55 ± 0.01	0.55 ± 0.01	0.79 ± 0.18	0.88 ± 0.04
	DC ± SD	0.18 ± 0.00	0.18 ± 0.00	0.17 ± 0.01	0.16 ± 0.01	0.18 ± 0.03	0.18 ± 0.01
Kittler	**ME ± SD (%)**	18.73 ± 0.40	19.44 ± 0.45	20.23 ± 0.68	21.64 ± 0.83	25.07 ± 1.28	27.65 ± 1.20
	FPR ± SD (%)	19.45 ± 0.41	20.19 ± 0.47	21.01 ± 0.71	22.48 ± 0.87	26.04 ± 1.33	28.72 ± 1.25
	FNR ± SD (%)	**0.54 ± 0.01**	**0.53 ± 0.01**	**0.53 ± 0.01**	**0.52 ± 0.01**	**0.51 ± 0.02**	**0.49 ± 0.02**
	DC ± SD	0.17 ± 0.00	0.16 ± 0.00	0.16 ± 0.00	0.15 ± 0.00	0.13 ± 0.01	0.12 ± 0.00
Local Mean	**ME ± SD (%)**	11.67 ± 0.22	12.07 ± 0.26	12.52 ± 0.37	13.33 ± 0.46	15.28 ± 0.71	16.96 ± 0.69
	FPR ± SD (%)	12.07 ± 0.23	12.48 ± 0.27	12.94 ± 0.39	13.78 ± 0.49	15.78 ± 0.75	17.51 ± 0.73
	FNR ± SD (%)	1.62 ± 0.19	1.72 ± 0.28	1.83 ± 0.31	2.00 ± 0.39	2.62 ± 0.58	2.99 ± 0.63
	DC ± SD	0.24 ± 0.00	0.24 ± 0.00	0.23 ± 0.01	0.22 ± 0.01	0.20 ± 0.01	0.18 ± 0.01
Bernsen	**ME ± SD (%)**	3.83 ± 0.15	4.11 ± 0.17	4.40 ± 0.24	4.94 ± 0.31	6.27 ± 0.53	7.41 ± 0.78
	FPR ± SD (%)	2.69 ± 0.16	2.95 ± 0.18	3.24 ± 0.26	3.78 ± 0.34	5.10 ± 0.60	6.24 ± 0.95
	FNR ± SD (%)	32.87 ± 0.44	33.30 ± 0.62	33.79 ± 0.81	34.33 ± 0.93	35.91 ± 2.39	37.17 ± 4.44
	DC ± SD	0.50 ± 0.01	0.47 ± 0.02	0.45 ± 0.02	0.41 ± 0.02	0.33 ± 0.02	0.29 ± 0.02

Table 4

Quantitative comparisons based on 100 simulated images generated from real image samples in Fig. 12.

	Criterion	DHR-RP	Otsu	Huang	Kittler	Local Mean	Bernsen
Low Vessel Density (Fig. 12a)	**ME ± SD (%)**	**4.01 ± 0.88**	5.73 ± 0.45	9.20 ± 0.91	18.32 ± 0.87	18.37 ± 0.78	6.22 ± 0.36
	FPR ± SD (%)	**3.65 ± 1.01**	5.46 ± 0.48	9.44 ± 0.94	18.84 ± 0.89	18.72 ± 0.81	4.77 ± 0.37
	FNR ± SD (%)	16.65 ± 7.62	15.04 ± 0.76	0.75 ± 0.05	**0.39 ± 0.02**	6.20 ± 0.31	56.66 ± 0.34
	DC ± SD	**0.41 ± 0.06**	0.31 ± 0.02	0.23 ± 0.02	0.13 ± 0.01	0.13 ± 0.00	0.21 ± 0.01
High Vessel Density (Fig. 12b)	**ME ± SD (%)**	**4.50 ± 0.69**	5.50 ± 0.51	10.70 ± 0.71	25.00 ± 0.69	18.73 ± 0.43	5.88 ± 0.27
	FPR ± SD (%)	**4.42 ± 0.81**	5.70 ± 0.54	11.20 ± 0.75	26.22 ± 0.72	19.53 ± 0.45	3.95 ± 0.28
	FNR ± SD (%)	6.13 ± 3.05	0.91 ± 0.02	0.63 ± 0.02	**0.31 ± 0.01**	2.54 ± 0.01	44.95 ± 0.37
	DC ± SD	**0.52 ± 0.04**	0.46 ± 0.02	0.30 ± 0.01	0.16 ± 0.00	0.20 ± 0.00	0.41 ± 0.02
Low Vessel Curvature (Fig. 12c)	**ME ± SD (%)**	**4.20 ± 0.57**	5.23 ± 0.53	13.34 ± 0.94	30.57 ± 0.98	19.02 ± 0.52	7.27 ± 0.31
	FPR ± SD (%)	**3.87 ± 0.67**	5.50 ± 0.57	14.12 ± 1.00	32.41 ± 1.04	19.70 ± 0.56	5.09 ± 0.32
	FNR ± SD (%)	9.69 ± 4.56	0.85 ± 0.10	0.38 ± 0.02	**0.14 ± 0.01**	7.81 ± 0.63	43.44 ± 0.77
	DC ± SD	**0.59 ± 0.04**	0.52 ± 0.03	0.30 ± 0.01	0.16 ± 0.00	0.22 ± 0.00	0.40 ± 0.02
High Vessel Curvature (Fig. 12d)	**ME ± SD (%)**	**4.37 ± 0.60**	6.15 ± 0.46	11.33 ± 0.76	27.28 ± 1.45	20.17 ± 0.44	5.38 ± 0.27
	FPR ± SD (%)	4.34 ± 0.67	6.32 ± 0.48	11.69 ± 0.79	28.19 ± 1.50	20.77 ± 0.46	**3.97 ± 0.28**
	FNR ± SD (%)	5.46 ± 3.09	1.08 ± 0.02	0.61 ± 0.02	**0.24 ± 0.02**	2.22 ± 0.25	47.24 ± 0.44
	DC ± SD	**0.43 ± 0.04**	0.34 ± 0.02	0.22 ± 0.01	0.11 ± 0.01	0.14 ± 0.00	0.31 ± 0.01
Low Branch Node Density (Fig. 12e)	**ME ± SD (%)**	**4.66 ± 0.79**	5.99 ± 0.49	9.43 ± 0.83	17.37 ± 0.99	18.36 ± 0.45	6.13 ± 0.31
	FPR ± SD (%)	**4.07 ± 0.99**	6.18 ± 0.51	9.78 ± 0.87	18.05 ± 1.03	18.95 ± 0.47	4.47 ± 0.32
	FNR ± SD (%)	19.18 ± 8.94	1.33 ± 0.09	0.85 ± 0.05	**0.44 ± 0.02**	3.53 ± 0.34	47.33 ± 0.65
	DC ± SD	**0.45 ± 0.05**	0.39 ± 0.02	0.29 ± 0.02	0.18 ± 0.01	0.17 ± 0.00	0.32 ± 0.02
High Branch Node Density (Fig. 12f)	**ME ± SD (%)**	**5.32 ± 0.49**	5.80 ± 0.39	11.54 ± 0.76	22.91 ± 0.95	17.89 ± 0.44	7.85 ± 0.25
	FPR ± SD (%)	**4.08 ± 0.68**	4.46 ± 0.51	12.37 ± 0.82	24.59 ± 1.03	18.63 ± 0.47	4.53 ± 0.26
	FNR ± SD (%)	21.94 ± 3.39	23.83 ± 1.39	0.45 ± 0.03	**0.21 ± 0.01**	7.93 ± 0.23	52.58 ± 0.32
	DC ± SD	**0.59 ± 0.04**	0.56 ± 0.03	0.38 ± 0.02	0.23 ± 0.01	0.38 ± 0.02	0.44 ± 0.02